

Insights into interfacial S-scheme/bulk type II dual charge transfer mechanism enabling silver oxide/N-rich carbon nitride anti-photocorrosion and enhanced photoactivity

Junlei Zhang ^{a,*}, Chaoyang Yang ^a, Hai Liu ^b, Guojia Yu ^a, Zhiyao Duan ^{a,*}, Shijie Li ^{c,*}

^a School of Materials Science and Engineering, State Key Laboratory of Solidification Processing, Atomic Control & Catalysis Engineering Laboratory, Northwestern Polytechnical University, Xi'an 710072, PR China

^b School of Environment, Guangzhou Key Laboratory of Environmental Exposure and Health, and Guangdong Key Laboratory of Environmental Pollution and Health, Jinan University, Guangzhou 510632, PR China

^c National Engineering Research Center for Marine Aquaculture, Zhejiang Ocean University, Zhoushan, Zhejiang 316022, PR China



ARTICLE INFO

Keywords:

Ag₂O/C₃N₅ heterojunction
Built-in electric field
Dual electron transfer mechanism
Anti-photocorrosion
Efficient water disinfection

ABSTRACT

Infectious diseases, such as COVID-19, continue to pose a significant threat to global public health and economics. This study establishes a one-of-a-kind heterojunction catalyst with a built-in electric field and enhanced structural defects, allowing for the formation of interfacial S-scheme and bulk type-II dual charge transfer channels, as demonstrated by extensive experimental investigation and density functional theory calculations. This unique property greatly enhances the photogenerated electron/hole pair separation and transfer, producing more active species in Ag₂O/C₃N₅ for water disinfection, which inactivation efficiency of *E. coli* is around 7.0 folds for pure C₃N₅ and 1.5 folds for Ag₂O. The spatial separation of photogenerated e⁻/h⁺ pairs and the tendency of O₂/H₂O molecules to be reduced or oxidized at the interface enable excellent anti-photocorrosion. Exceptional disinfection of real lake and river water, along with exceptional stability and reusability, demonstrate the practical application potential. This work is pivotal for the theoretical development of sophisticated photocatalytic systems.

1. Introduction

Until recently, the ongoing threat of infectious diseases posed a significant burden on global public health and economics, for example, the corona virus disease 2019 (COVID-19) has resulted in high casualties due to subsequent bacterial infections, implying that infection illnesses remain a major concern around the world [1,2]. Photocatalysis has developed as a successful and promising antimicrobial technique in recent years due to its ability to employ green solar energy to create reactive oxygen species (ROS) or other active species for the destruction of a range of harmful microorganisms such as bacteria, viruses, and others [3,4]. To reach the "double carbon" targets, it is required and critical to develop high-efficiency and stable photocatalysts.

Building heterojunctions has been emerging as an efficient strategy for developing superior photocatalysts [5–7], this is because that separation/transfer of photoexcited electrons (e⁻) and holes (h⁺) can be reinforced through spatial isolation, thereby giving birth to more active

species for disinfection. From early UV-response to visible-light responsive semiconductor-based heterojunction catalysts that are widely studied today, one clear development trend is to design and develop high-efficiency heterojunction photocatalysts than can work under visible light [8–17], because such catalysts not only can more effectively utilize solar energy but also exhibit the higher efficiency of separation and transfer of photoexcited carriers.

Just as of lately, nitrogen-rich polymer carbon nitride of C₃N₅ is gaining much attention in the photocatalytic field due to the relatively narrow bandgap (~1.9 eV), abundant structural defects, good thermal stability, and environmental friendliness [18–21]. To conquer the drawbacks of serious recombination of photogenerated carriers, heterostructure regulation is also used to improve pristine C₃N₅ [22–24]. Generally speaking, after forming a heterojunction, difference in Fermi energy levels results in the change of energy band structures of semiconductors comprising a heterojunction to balance the Fermi energy level, thereby creating a built-in electric field among different

* Corresponding authors.

E-mail addresses: junlei@nwpu.edu.cn (J. Zhang), zhiyao.duan@nwpu.edu.cn (Z. Duan), lishijie@zjou.edu.cn (S. Li).

semiconductors [24–28]. Driven by a built-in electric field, the transfer pathways of photogenerated carriers may be quite different, thus leading to different catalytic activities [29–31]. Such in-depth understanding is a further development of the theory of heterojunction photocatalysis. Nevertheless, corresponding awareness needs to be further enhanced and deepened, for instance, all of semiconductors comprising a heterojunction may have a defect energy level, which might result in a multi-pathway transfer mechanism of photogenerated carriers. However, very few relevant studies have explored this issue in depth. Furthermore, silver oxide (Ag_2O), as a typical p-type semiconductor with electron density waves that can be easily initiated by light waves, has emerged as a significant photocatalyst [32]. In terms of its relative narrow band gap (around 1.3 eV) [33], it usually is used to modify other semiconductors such as TiO_2 [34–36], CeO_2 [37], Bi_2WO_6 [38], g- C_3N_4 [39], etc. for improving visible light response and inhibiting the recombination of photogenerated carriers, thereby resulting in better photocatalytic activity. Unfortunately, phenomenon on the multi-pathway transfer mechanism of photogenerated carriers in a heterojunction photocatalyst is still not paid attention to and studied. Furthermore, work on coupling with Ag_2O to enhance C_3N_5 's photocatalytic activity has not yet been made available.

Taking silver oxide/N-rich carbon nitride as a new case heterojunction photocatalyst, this work for the first time demonstrates the co-existence of dual charge transfer pathways in a heterojunction. Detailed characterizations validate the built-in electric field between C_3N_5 and Ag_2O as well as the defect energy levels in C_3N_5 and Ag_2O . In-depth density functional theory (DFT) calculations demonstrate the energy-structure relationship of C_3N_5 and Ag_2O after contact. Such above facts suggest that under visible light irradiation, interfacial S-scheme and bulk Type II dual charge transfer pathways driven by the built-in electric field coexist in the $\text{Ag}_2\text{O}/\text{C}_3\text{N}_5$ heterojunction. Without a doubt, $\text{Ag}_2\text{O}/\text{C}_3\text{N}_5$ exhibits a significantly upgraded photocatalytic water disinfection performance compared to pristine C_3N_5 and Ag_2O . Moreover, excellent anti-photocorrosion property caused by the spatial isolation of photogenerated e^- to C_3N_5 endows $\text{Ag}_2\text{O}/\text{C}_3\text{N}_5$ with a superior reusability. This study presents a new and remarkable catalyst for photocatalytic water disinfection by constructing a dual-charge-transfer route, which gives a vital reference for the creation of high-efficiency photocatalysts.

2. Experimental section

2.1. Synthesis of $\text{Ag}_2\text{O}/\text{C}_3\text{N}_5$

Synthesis procedure of $\text{Ag}_2\text{O}/\text{C}_3\text{N}_5$ heterojunction catalysts is illustrated in [Scheme S1](#). Firstly, according to previous report [40], bulk C_3N_5 was prepared by calcining 1.6 g 3-amino-1,2,4-triazole in a muffle furnace at 500 °C for 3 hours, and after grounding into uniform powder for further use. Secondly, Ag_2O nanoparticles were anchored on C_3N_5 by a chemical adsorption-deposition procedure. [41] Typically, a certain amount of Ag^+ solution was dropwise added into 50 mL of C_3N_5 suspension, continuously stirring for 3 hours at 60 °C to saturation adsorption. After that, the same molar amount of NaOH solution was dropped into above mixed suspension drop by drop, continuously stirring for another 3 hours at 60 °C to complete the formation of Ag_2O . Lastly, about three wash treatment operations using deionized water were conducted for removing residue Na^+ , and the obtained powder was dried in an oven at 60 °C for further use. We got four $\text{Ag}_2\text{O}/\text{C}_3\text{N}_5$ samples with varying Ag_2O contents by varying the Ag^+ dose; these samples are referred to as $\text{Ag}_2\text{O}/\text{C}_3\text{N}_5\text{-1}$, $\text{Ag}_2\text{O}/\text{C}_3\text{N}_5\text{-2}$, $\text{Ag}_2\text{O}/\text{C}_3\text{N}_5\text{-3}$, and $\text{Ag}_2\text{O}/\text{C}_3\text{N}_5\text{-4}$, respectively. Furthermore, we validated the Ag_2O contents in four $\text{Ag}_2\text{O}/\text{C}_3\text{N}_5$ samples (1.5 wt%, 3.5 wt%, 5.3 wt%, and 8.2 wt%, respectively) using the ICP-MS (Agilent 7800) technique ([Figure S1](#)).

2.2. Photocatalytic disinfection experiments

Under visible light ($\lambda > 420$ nm) radiation, the photocatalytic water disinfection activity of as-prepared catalysts was investigated. The light source was a 300 W Xe lamp (PLS-SXE300+, Beijing Perfectlight Technology Co., Ltd.) with a UV-cut off filter (420 nm). Add 2 mg catalyst to 100 mL bacterial suspension (10^7 CFU/mL) and mix for 30 minutes in the dark. After taking the blank sample, the combined solution was exposed to visible light to begin the studies. A low temperature constant temperature stirring reaction bath was employed during the experiment to maintain the ambient temperature and stirring rate of 200 rpm. At 2.5, 5, 7.5, 10, 15, and 20 min, 1 mL of the combined solution was removed, and the bacteria were grown and counted. When testing the influence of pH on photocatalytic disinfection, the starting pH of the reaction system was 5.5, which was adjusted using NaOH and Na_2SO_4 . Each experiment was carried out three times.

In addition, four recycling tests and once-regenerated experiments were performed to assess the stability and reusability of $\text{Ag}_2\text{O}/\text{C}_3\text{N}_5$. For the former, the wasted $\text{Ag}_2\text{O}/\text{C}_3\text{N}_5$ sample must be thoroughly cleaned with deionized water for further recycling use; for the latter, the spent $\text{Ag}_2\text{O}/\text{C}_3\text{N}_5$ sample must be calcined at 300 °C for 1 hour after the fourth run.

2.3. Density functional theory (DFT) calculations

We performed spin-polarized density of functional theory (DFT) calculations using the projector-augmented wave (PAW) method [42] as implemented in the Vienna ab initio simulation package (VASP) [43–45]. An energy cutoff of 400 eV for the plane wave basis set was used to expand the Kohn-Sham orbitals. The generalized gradient approximation (GGA) with the Perdew-Burke-Ernzerh (PBE) functional [46] was employed to describe the exchange and correlation energy. Due to the well-known problem of GGA in underestimating the band gap of semiconductors, we also employed hybrid density functional proposed by Heyd, Scuseria, and Ernzerhof (HSE06) [47] that corrects, to a large part, the band gap underestimation [48]. Due to the large computational load, DFT-HSE06 was only used for evaluating the electronic structure based on the structure optimized on the DFT-PBE level. Grimme's method (DFT-D3) was employed to account for the Van der Waals interactions. Convergence criteria of 10^{-5} eV were used for the electronic relaxations. The atomic structures were considered fully relaxed until the residual force on each atom is less than 0.05 eV/Å.

The unit cell of Ag_2O is cubic and its lattice constant is calculated to be $a = 4.809$ Å ([Figure S3](#)). The nearest neighbor Ag-O and Ag-Ag bond lengths are 2.081 Å and 3.485 Å, respectively. A Monkhorst-Pack k-point mesh [49] of $12 \times 12 \times 12$ is used for the unit cell optimization. Ag_2O nanocluster was modeled by a truncated cube, which is enclosed by (100) and (110) surface groups as shown in [Figure S3a](#). The Ag_2O nanocluster consists of 96 Ag and 67 O atoms. After relaxation, the Ag_2O nanocluster exhibits a rounded shape as can be seen in [Figure S3b-c](#). The atomic structure of C_3N_5 is shown in [Figure S4](#), which has a disordered atomic arrangement. The dimension of the supercell is $5.65 \text{ \AA} \times 6.69 \text{ \AA} \times 15.0 \text{ \AA}$. Along z direction, a vacuum layer of 15 Å in thickness is introduced to avoid the interaction between neighboring images. A single Γ point is used for the calculations of Ag_2O nanocluster and C_3N_5 .

The adsorption ability of $\text{Ag}_2\text{O}/\text{C}_3\text{N}_5$ for O_2 and H_2O molecules is determined by adsorption energies (E_{ads}) calculations, where $E_{\text{ads}} = E_{\text{ad}}/ \text{sub} - E_{\text{ad}} - E_{\text{sub}}$, where $E_{\text{ad}/\text{sub}}$, E_{ad} , and E_{sub} are the optimized adsorbate/substrate combined system, the adsorbate in the structure and the clean substrate respectively. A more negative E_{ads} value reflects a stronger adsorption.

3. Results and discussion

3.1. Catalyst heterostructure building and characterization

To realize the upgradation of photoactivity for water disinfection, we employed the facile chemical adsorption-deposition procedure to synthesize $\text{Ag}_2\text{O}/\text{C}_3\text{N}_5$ samples with various Ag_2O loadings (Fig. 1a and Scheme S1). Firstly, transmission electron microscope (TEM) image shown in Fig. 1b clearly shows that $\text{Ag}_2\text{O}/\text{C}_3\text{N}_5$ is composed of nanoparticles and nanosheets, and the former are dispersed well on the latter. By size statistics, it can be seen from Fig. 1c that size distribution of nanoparticles is mainly below 20 nm, and the average size is around 15 nm. Further high-resolution TEM image confirms that the nanoparticles belong to Ag_2O by the obvious lattice stripes with a spacing of 0.335 nm ascribed to the (110) crystal plane of cubic Ag_2O , and the nanosheets should be attributed to amorphous C_3N_5 (Fig. 1d). High-angle annular dark-field (HAADF) STEM (Figure S5a) and the corresponding elemental mapping images (Fig. 1e) well demonstrate the morphology structure and the uniform dispersion of C/N/Ag/O four elements. In addition, the existence of C/N/Ag/O four elements in $\text{Ag}_2\text{O}/\text{C}_3\text{N}_5$ is also validated by the energy-dispersive X-ray spectroscopy (EDS) spectrum shown in Figure S5b.

X-ray diffraction (XRD) patterns presented in Fig. 2a and Figure S6a were collected for the analysis of phase composition [50]. From the higher Ag_2O loading of 8.2 wt%, analysis in conjunction with the standard XRD pattern demonstrates that cubic Ag_2O (PDF#43-0997) is in $\text{Ag}_2\text{O}/\text{C}_3\text{N}_5$ samples, and from the XRD spectrum of $\text{Ag}_2\text{O}/\text{C}_3\text{N}_5$ _4, it can clearly observe the diffraction peaks belonging to the crystal plane (111), (200), (220), and (311) of standard cubic Ag_2O , respectively [51]. Importantly, when the Ag_2O loading is less than or equal to 5.3 wt%, no obvious diffraction peaks are observed, demonstrating the Ag_2O species are highly dispersed in $\text{Ag}_2\text{O}/\text{C}_3\text{N}_5$. Furthermore, to further confirm the composition of C_3N_5 , we analyzed the mass ratio of as-prepared C_3N_5

sample on an organic element analyzer (Elementar Vario EL). As shown in Figure S6, two testing data of C/N mass ratio are 0.557 and 0.556, respectively, which are very close to that theoretical value 0.550. In the latest report by Li et al. [52], the authors used the solid-state ^{13}C and ^{15}N NMR spectra to clearly identify and demonstrate the molecular structure of C_3N_5 prepared by the same method reported by us in 2021 [40]. Further combined with reported research results [20,40,52], it can well confirm the reasonableness and accuracy of the molecular structure of C_3N_5 mentioned in this work. XRD results are well consistent with the observation by TEM and elemental mapping images (Fig. 1b and d-e), further demonstrating that the $\text{Ag}_2\text{O}/\text{C}_3\text{N}_5$ sample consist of Ag_2O nanoparticles and C_3N_5 nanosheets. Furthermore, from Fig. 2a and S7, it can be seen that after anchoring Ag_2O nanoparticles on C_3N_5 nanosheets, the diffraction peak belonging to the crystal plane (002) of C_3N_5 shows a red shift, and increasing Ag_2O loading results in the larger redshift, indicating that the procedure introducing Ag_2O destroys bulk C_3N_5 , resulting in a smaller size, and a higher Ag_2O loading leads to a smaller size of C_3N_5 , which may be attributed to the intercalation effect of more Ag_2O nanoparticles. Such above results demonstrate an intrinsic interaction between Ag_2O nanoparticles and C_3N_5 nanosheets.

X-ray photoelectron spectroscopy (XPS) spectra were further used to analyze and confirm the elemental composition and surface element chemical valence states of as-prepared catalysts [53]. Survey XPS spectra (Figure S8) confirm the co-existence of four elements including Ag, O, C, and N on $\text{Ag}_2\text{O}/\text{C}_3\text{N}_5$ _3, being consistent with above TEM and XRD results. Further high-resolution XPS spectra of C 1 s and N 1 s (Fig. 2b-c) confirm the N=C-N, C=N-C, N-(C)₃, and C-N-H functional groups, demonstrating the C-N frame in C_3N_5 , well agreeing with the previous studied results [20,54,55]. In addition, observed C=C and C-O groups ascribe the surface carbon contamination [56]. As can be verified from Fig. 2d, there are only Ag^+ species on $\text{Ag}_2\text{O}/\text{C}_3\text{N}_5$ _3, but the difference is that the binding energy is shifted to lower values compared to pristine Ag_2O , confirming a strong electron interaction between Ag_2O

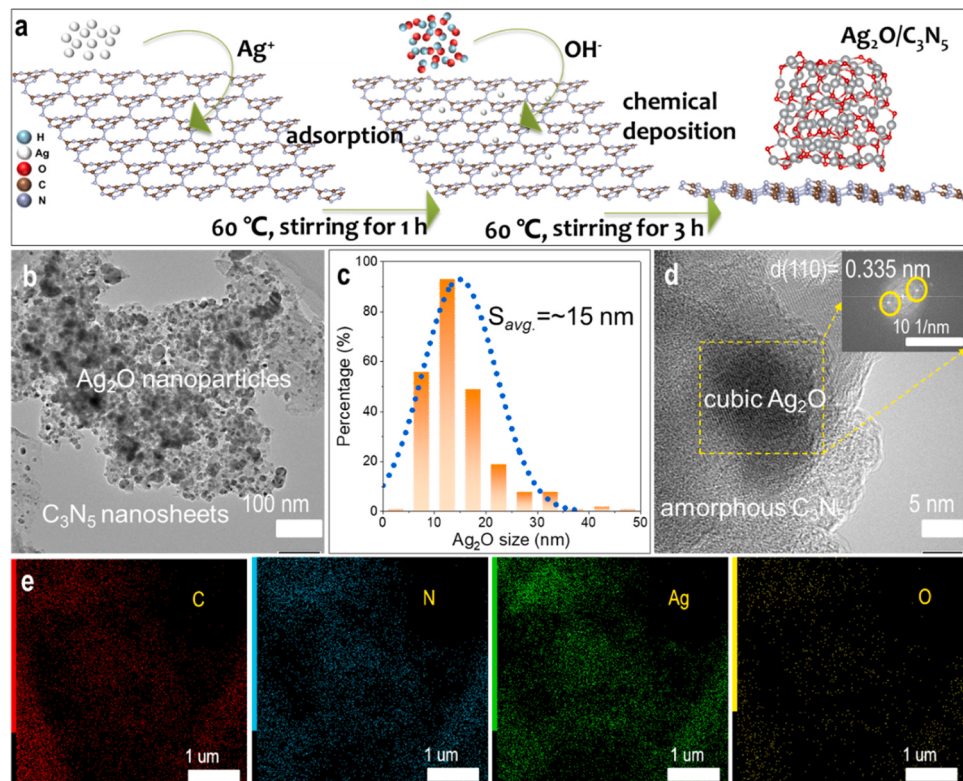


Fig. 1. (a) Schematic diagram for the synthesis of $\text{Ag}_2\text{O}/\text{C}_3\text{N}_5$. (b) Transmission electron microscope (TEM), (c) the size distribution of Ag_2O nanoparticles, and (d) high-resolution TEM images of $\text{Ag}_2\text{O}/\text{C}_3\text{N}_5$ _3 (inset shows the fast Fourier transform (FFT) image of selected area). (e) EDX elemental mappings of C, N, Ag, and O in $\text{Ag}_2\text{O}/\text{C}_3\text{N}_5$ _3.

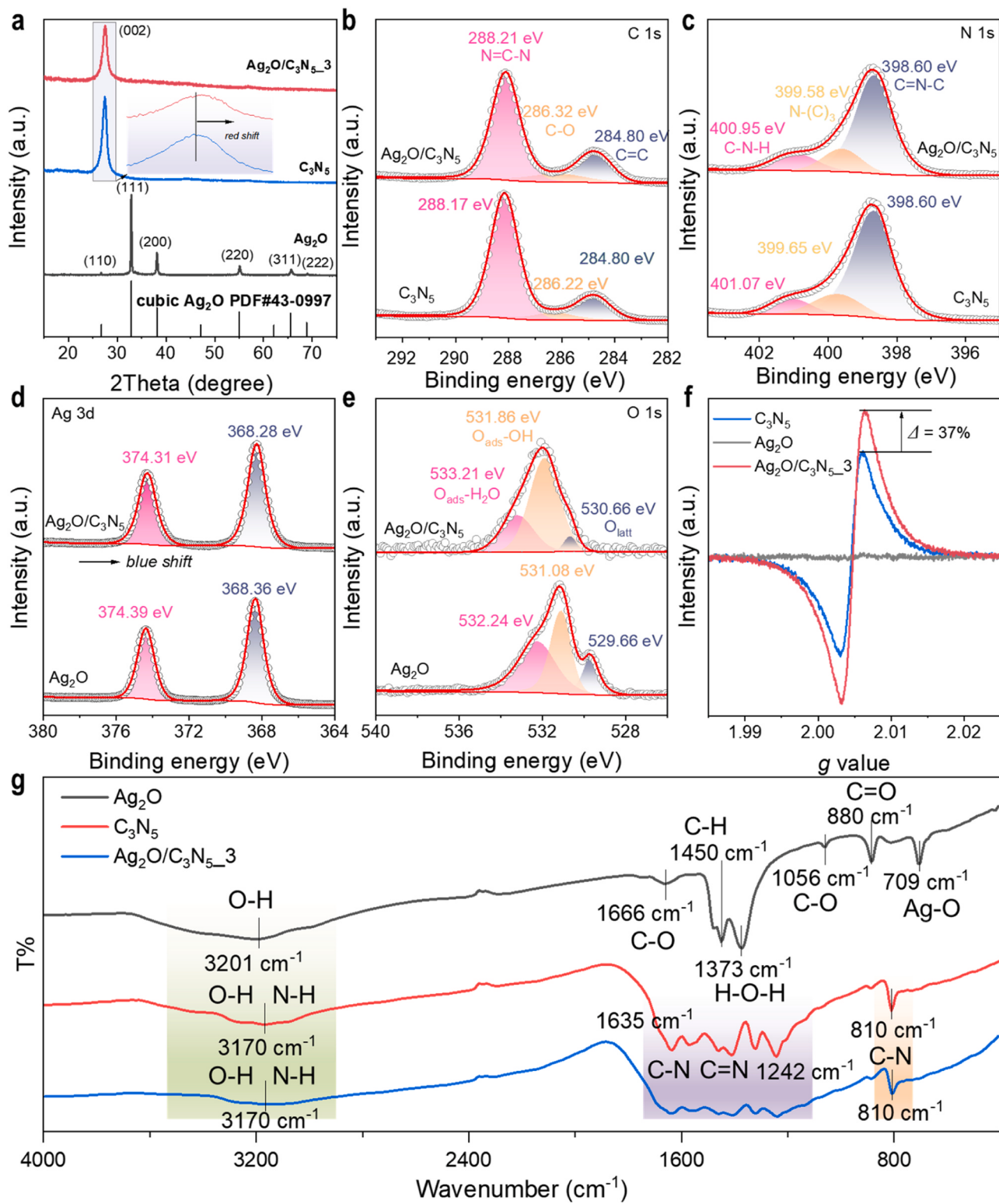


Fig. 2. (a) X-ray diffraction (XRD) patterns of as-prepared Ag_2O , C_3N_5 , and $\text{Ag}_2\text{O}/\text{C}_3\text{N}_5\text{-}3$ samples as well as the standard XRD pattern of cubic Ag_2O (PDF#43-0997). (b-e) High-resolution X-ray photoelectron spectroscopy (XPS) spectra of C 1s, N 1s, Ag 3d, and O 1s. (f) electron spin resonance (ESR) and (g) Fourier transform infrared (FTIR) spectra of Ag_2O , C_3N_5 , and $\text{Ag}_2\text{O}/\text{C}_3\text{N}_5\text{-}3$.

and C_3N_5 , and the direction of built-in electric field is from C_3N_5 to Ag_2O [57]. Furthermore, lattice oxygen (O_{latt}) and adsorbed oxygen ($\text{O}_{\text{ads}}\text{-OH}/\text{H}_2\text{O}$) species are figured out (Fig. 2e) on $\text{Ag}_2\text{O}/\text{C}_3\text{N}_5\text{-}3$, which well demonstrates the fact of Ag_2O on C_3N_5 [58]. The further comparable analysis results of the relative percentages of different functional groups (Figure S9) on one hand suggest that depositing Ag_2O on C_3N_5

can eliminate part of adsorbed contaminated carbon species for better exposure of C-N frames, thereby resulting in more active sites, and more importantly, the significant reduction of O_{latt} species and increase of $\text{O}_{\text{ads}}\text{-OH}$ make a strong case for the generation of oxygen vacancies in Ag_2O after combining with C_3N_5 . Further electron spin resonance (ESR) spectra (Fig. 2f) indicate that pristine Ag_2O has no structural defects, but

after coupling with C_3N_5 , $\text{Ag}_2\text{O}/\text{C}_3\text{N}_5\text{-}3$ exhibits 37% of increased structural defects compared to C_3N_5 [50], which demonstrates the fact that C_3N_5 can promote the dispersion of Ag_2O nanoparticles and the generation of oxygen vacancies.

Moreover, Fourier-transform infrared spectroscopy was used to perform the characterization and validation of surface functional groups on Ag_2O , C_3N_5 , and $\text{Ag}_2\text{O}/\text{C}_3\text{N}_5\text{-}3$ [51,57]. As shown in Figure 2 g, there are four types of functional groups on as-prepared pure Ag_2O : O-H/H-O-H, C-O/C=O, C-H, and Ag-O. The first three are attributed to surface adsorbed H_2O and CO_2 molecules, while the latter is caused by Ag_2O , demonstrating Ag_2O 's composition and adsorption ability for H_2O and CO_2 molecules. On as-prepared pure C_3N_5 , the obvious peaks caused by the N-H and O-H stretching vibrations, CN heterocyclic stretching vibrations, and s-triazine ring vibration are observed, which well agrees with previous reports [54,57,59], demonstrating the composition of C_3N_5 . The as-prepared $\text{Ag}_2\text{O}/\text{C}_3\text{N}_5\text{-}3$ sample has nearly the same surface functional groups as pure C_3N_5 , and there is no obvious peak corresponding to the Ag-O stretching vibration, but it is clear that peaks caused by the CN heterocyclic stretching and s-triazine ring vibrations decrease in intensity after loading Ag_2O . Such results are consistent with the conclusions from XRD, TEM, and XPS data, *viz.*, Ag_2O nanoparticles are highly uniformly distributed on C_3N_5 nanosheets, and there is a strong electric interaction between Ag_2O and C_3N_5 as verified by the identification of the built-in electric field. Further, the fact that both of Ag_2O and C_3N_5 in $\text{Ag}_2\text{O}/\text{C}_3\text{N}_5$ have structural defects is demonstrated. Overall, such unique properties may enable $\text{Ag}_2\text{O}/\text{C}_3\text{N}_5$ better separation and transfer of photogenerated carriers, thereby resulting in a superior photoactivity.

3.2. Analysis on the optical properties

In general, heterostructure building promotes the electron transfer

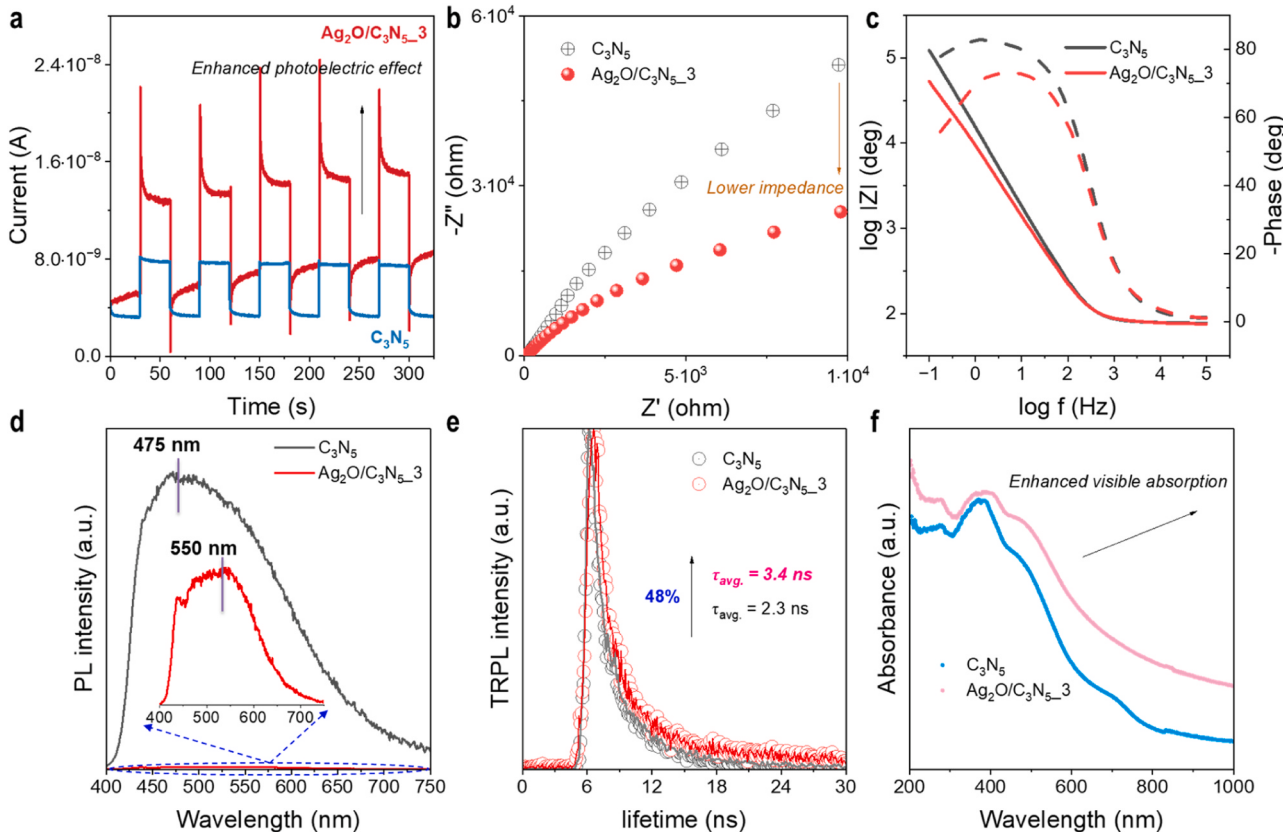


Fig. 3. (a) Transient photocurrent responses, (b) Electrochemical impedance spectroscopy (EIS) Nyquist plots, (c) Log $|Z|$ and Bode phase plots, (d) photoluminescence (PL) spectra, (e) time-resolved PL decay spectra, and (f) UV-vis NIR diffuse reflectance spectra belonging to C_3N_5 and $\text{Ag}_2\text{O}/\text{C}_3\text{N}_5\text{-}3$.

collected and fit using a formula of $R(t) = B_1 e^{(-t/t_1)} + B_2 e^{(-t/t_2)} + B_3 e^{(-t/t_3)} + B_4 e^{(-t/t_4)}$ to calculate the lifetime of $\text{Ag}_2\text{O}/\text{C}_3\text{N}_5$, 3, C_3N_5 , and Ag_2O , which are around 3.4 ns, 2.3 ns, and 4.2 ns, respectively (Fig. 3e and S12). Such clear results well agree with the conclusion of PL spectra. In addition, adding Ag_2O shifts the PL emission peak from approximately 475 nm to near 550 nm (Fig. 3d), implying that adding Ag_2O provides an additional energy level that can absorb and utilize light with a longer wavelength [65].

UV-vis NIR diffuse reflectance spectra were subsequently used to study the light-response behavior of $\text{Ag}_2\text{O}/\text{C}_3\text{N}_5$ -3, C_3N_5 , and Ag_2O (Fig. 3f and S13a). Clearly, introducing Ag_2O with a narrower bandgap of around 1.60 eV (Figure S13b) can make a $\text{Ag}_2\text{O}/\text{C}_3\text{N}_5$ heterojunction

catalyst (e.g., $\text{Ag}_2\text{O}/\text{C}_3\text{N}_5$ -3) with obviously enlarged the range of visible response compared to pristine C_3N_5 (bandgap: ~ 1.95 eV), which is beneficial to the utilization efficiency of visible light, might enabling a better photoactivity.

3.3. Photocatalytic performance for water disinfection

Selecting *Escherichia coli* (*E. coli*, 10^7 CFU/mL) as the model bacterium to evaluate the photocatalytic performance of as-prepared $\text{Ag}_2\text{O}/\text{C}_3\text{N}_5$ catalysts in water disinfection. As illustrated in Fig. 4a, in dark, $\text{Ag}_2\text{O}/\text{C}_3\text{N}_5$ -3 sample exhibits a negligible *E. coli* inactivation during a 20 min of reaction, while upon introducing visible light, *E. coli* in water

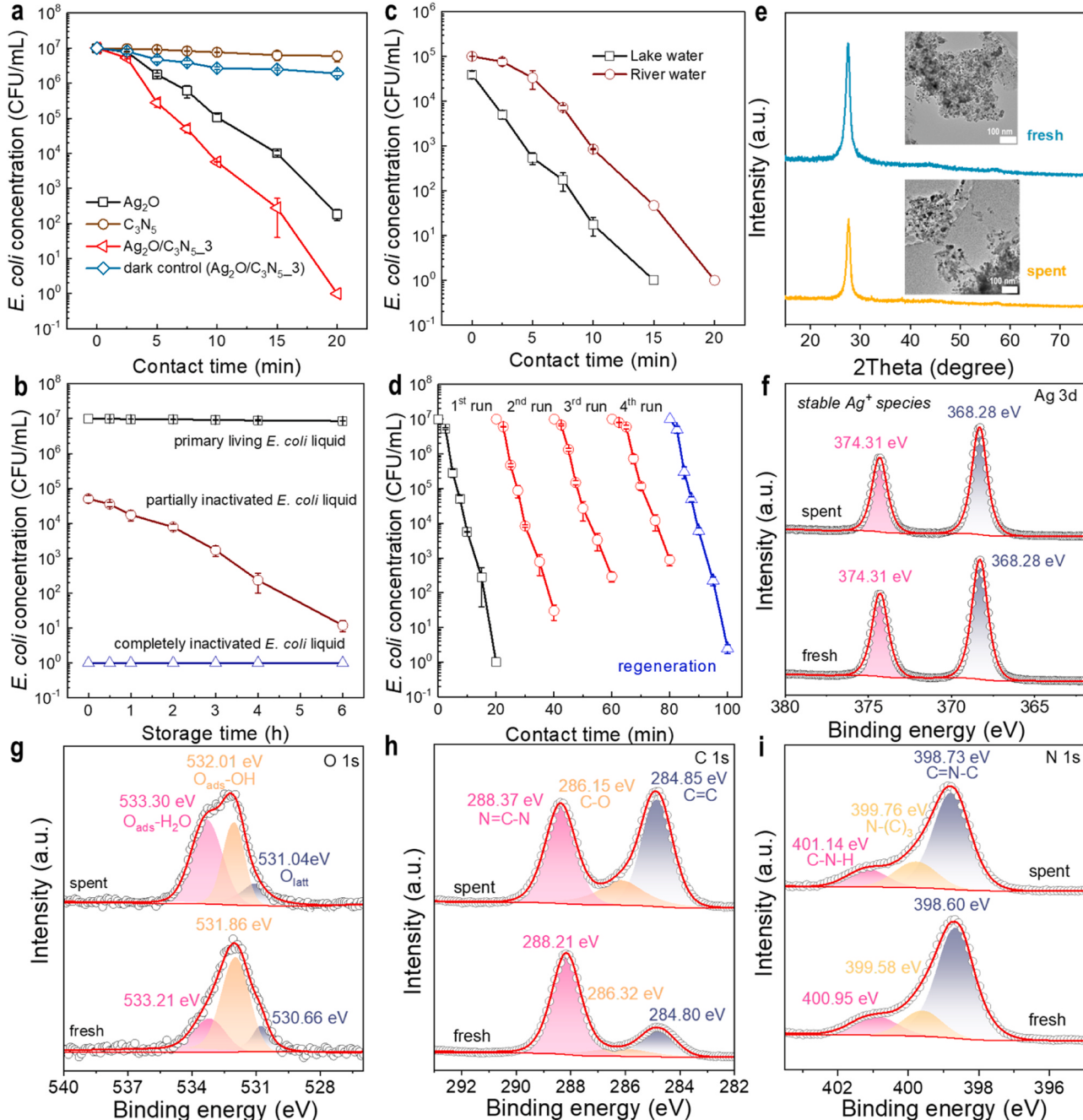


Fig. 4. (a) Bacterial inactivation (*E. coli*, 10^7 CFU/mL) in 100 mL solution by the $\text{Ag}_2\text{O}/\text{Vis}$, $\text{C}_3\text{N}_5/\text{Vis}$, $\text{Ag}_2\text{O}/\text{C}_3\text{N}_5$ -3/Vis or $\text{Ag}_2\text{O}/\text{C}_3\text{N}_5$ -3 reaction systems. (b) The change trend of *E. coli* concentration in primary living, partially inactivated, and completely inactivated bacterial solutions in dark. (c) Actual water disinfection performance of the $\text{Ag}_2\text{O}/\text{C}_3\text{N}_5$ -3/Vis system. (d) Four recycling and once regeneration experiments of $\text{Ag}_2\text{O}/\text{C}_3\text{N}_5$ -3 sample. (e-i) XRD patterns (inset shows the TEM images of fresh and spent samples) and high-resolution XPS of Ag 3d/ O 1s/ C 1s/ N 1s of fresh and spent $\text{Ag}_2\text{O}/\text{C}_3\text{N}_5$ -3 samples.

rapidly inactivate and at 20 min, completely inactivate. The fluorescence microscopic images (Figure S14) of *E. coli* = 10⁷ CFU/mL treated by the Ag₂O/C₃N₅_3/Vis system with 0, 2, and 20 min further verify the excellent photocatalytic water disinfection of Ag₂O/C₃N₅_3 [66]. Furthermore, Ag₂O/C₃N₅_3 exhibits a remarkably superior to pristine C₃N₅ and Ag₂O. These results demonstrate that heterostructure empowers Ag₂O/C₃N₅ enhanced photocatalytic activity in comparison to single-component Ag₂O or C₃N₅. In addition, the loading control of Ag₂O on C₃N₅ was performed for the optimization of performance (Figure S15). It was found that optimal percentage of Ag₂O in Ag₂O/C₃N₅ is 5.3 wt%, and at this point, the Ag₂O/C₃N₅ heterostructure was optimally optimized.

Moreover, to confirm the real photocatalytic water disinfection effect of Ag₂O/C₃N₅_3, immediately after the photocatalytic disinfection is finished, we use aluminum foil to block out the light and keep it on for 6 hours (Fig. 4b). It is pretty clear that no resurrection occurs after completely photocatalytic disinfection, and even the partially inactivated bacteria liquid, *E. coli* inactivates gradually. In contrast, the concentration of *E. coli* in primary living bacteria liquid keeps unchanged. Such facts well demonstrate the excellent ability of Ag₂O/C₃N₅_3 in water disinfection. The practical water disinfection ability of Ag₂O/C₃N₅_3/Vis system is proved by employing the actual lake and river water samples (Fig. 4c), and within 20 min of reaction, *E. coli* in lake or river water completely inactivate.

To demonstrate the superior capability of the Ag₂O/C₃N₅_3/Vis system in inactivating *E. coli*, we investigated and compared the performance of twenty-three previously reported heterojunction catalysts containing Ag or carbon nitride in visible-light-driven *E. coli* inactivation. As shown in Figure S16 and Table S1, it can be clearly seen that the performance of the Ag₂O/C₃N₅_3/Vis system exceeds nearly all reported visible-light catalytic systems except the edge-functionalized C₃N₄/Vis system, and the performance of the Ag₂O/C₃N₅_3/Vis and edge-functionalized C₃N₄/Vis systems is almost the same. Such a fact well demonstrates the great potential of the Ag₂O/C₃N₅_3/Vis system in efficiently inactivating *E. coli*, which contributes to the development of advanced water disinfection technology.

Stability of a photocatalyst usually determines its application potential. Therefore, a four-cycle test by reusing Ag₂O/C₃N₅_3 was carried out (Fig. 4d). It can be found that the inactivated *E. coli* (Log₁₀(C₀/C_t)) at 20 min decreases from 7 for the first run down to around 4.0 for the fourth run. Such decline can ascribe the masking of the active site by the substances including various kinds of biomacromolecules, organic compounds, and cations and small molecules within cells released into the reaction system caused by the cell membrane damage [17,67,68]. To address this problem, we regenerated spent Ag₂O/C₃N₅_3 sample by calcining the spent sample at 300 °C for 1 h. Fortunately, the photocatalytic *E. coli* inactivation performance (Log₁₀(C₀/C_t)) of spent Ag₂O/C₃N₅_3 is restored to 6.6, very closing to the 7 for the first run. Such above results demonstrate the reusability of Ag₂O/C₃N₅_3 in photocatalytic water disinfection. From Fig. 4e, stable phase and morphology structures of Ag₂O/C₃N₅_3 are verified before and after reuse. Survey XPS spectra (Figure S17) further confirm the stable element composition. More importantly, high-resolution XPS spectra of Ag 3d on fresh and spent Ag₂O/C₃N₅_3 (Fig. 4f) are well able to prove the photocorrosion resistance of Ag₂O, *viz.*, no change from Ag⁺ reduction to Ag⁰ occurs. After the reaction, the three kinds of O species (Fig. 4g and S18a) (O_{latt.}, O_{ads}-OH, and O_{ads}-H₂O) show increasing, decreasing, and increasing changes, respectively. The aqueous phase reaction environment is responsible for the increased O_{ads}-H₂O, while the decrease of O_{ads}-OH might be attributed to its desorption to generate ·OH for water disinfection, and for the increase of O_{latt.}, it might be the progress of H₂O to ·OH. From Fig. 4h and S18b, the obviously increased C=C and C-O species on one hand support the above results of O_{ads}-H₂O species increase, on other hand, which can also demonstrate the fact that intermediates deposit on the surface active sites of Ag₂O/C₃N₅_3. Moreover, combining with the slight

change of N species (Fig. 4i and S18c), it can conclude that Ag₂O/C₃N₅_3 remains a stable Ag₂O and C₃N₅ composition in reuse.

3.4. Photocatalytic mechanism for water disinfection

In order to elucidate the reaction mechanism photo-catalyzing water disinfection by Ag₂O/C₃N₅ heterojunction catalyst, we further adopted systematic density functional theory (DFT) calculations to determine the energy band structure of Ag₂O and C₃N₅ in Ag₂O/C₃N₅ heterojunction. Firstly, the work function values of Ag₂O and C₃N₅ are calculated to be 5.973 eV and 5.578 eV, respectively (Fig. 5a). Higher work function means a lower Fermi energy level [69]. Therefore, after C₃N₅ contacting with Ag₂O, to balance the Fermi energy level, electron transfer from C₃N₅ to Ag₂O will occur, thereby building an internal electric field with a direction from C₃N₅ to Ag₂O (Fig. 5d), which is consistent with the result from the XPS data analysis (Fig. 2d). From Fig. 5b, the charge density difference and the corresponding planar-average charge density are further calculated around the interface of Ag₂O/C₃N₅. It is found that extra charge skews towards Ag₂O around the interfacial site, verifying the built-in field in Ag₂O/C₃N₅ as illustrated in Fig. 5d. Furthermore, by analyzing the total density of states (DOS) of Ag₂O and C₃N₅ in Ag₂O/C₃N₅ heterojunction (Fig. 5c), it can be seen that C₃N₅ has a more negative conduction band energy level than Ag₂O at the interface, which can be attributed to the antibonding orbitals built from Ag-dz² and O-2p orbitals. Moreover, according to reported studies [22,70], it is well known that Ag₂O and C₃N₅ are a typical p-type semiconductor and n-type semiconductor, respectively. When p-type Ag₂O comes into contact with n-type C₃N₅, the diffusion of electrons and holes leads to the formation of a p-n junction with a space charge region at the interface, resulting in a built-in potential that can direct electron and hole movement in opposite directions. Furthermore, due to the Fermi level collaboration, the p-type semiconductor's energy band raises as compared to the n-type semiconductor [71–74]. On base of above DFT calculations and p-n heterojunction formation theory, the energy band structures of Ag₂O and C₃N₅ in Ag₂O/C₃N₅ are verified as shown in Fig. 5d.

Based on above analysis, under visible light irradiation, driven by built-in electric field, photogenerated electrons (e⁻) jumping to the defect site of Ag₂O cannot flow to that of C₃N₅ but into the interfacial electric field to recombine with the holes (h⁺) coming from the valence band (VB) of C₃N₅, thereby forming a interfacial S-scheme charge transfer channel. On the other hand, since the more negative conduction band (CB) potential of Ag₂O, the photogenerated electrons (e⁻) jumping to the CB of Ag₂O will rapidly transfer to the CB of C₃N₅ under the force of the built-in electric field, and at the same time, the holes (h⁺) left in the VB of C₃N₅ will also rapidly transfer to the VB of Ag₂O, lastly building a bulk Type II charge transfer channel. In brief, under visible light irradiation, two kinds of charge transfer channels, *viz.*, interfacial S-scheme and bulk Type II, will work simultaneously in Ag₂O/C₃N₅ heterojunction (Fig. 5d).

Such a special electron transfer mechanism on one hand accelerates the separation and transfer of photogenerated carriers, spawning more electrons (e⁻) and holes (h⁺) to participate in subsequent photocatalytic reaction, and on the other hand, the spatial separation of photogenerated electrons (e⁻) and holes (h⁺), *viz.*, the electrons (e⁻) are predominantly enriched in C₃N₅, while the holes (h⁺) concentrate in Ag₂O, protect Ag₂O in Ag₂O/C₃N₅ heterojunction from reduction, achieving resistance to photocorrosion [32].

Further, electron spin resonance (ESR) spin-trapping tests were conducted for the identification of active species responsible for photocatalytic performance [75]. From Fig. 6a, it can be easily observed that ESR signal intensity of TEMPO-h⁺ by using Ag₂O/C₃N₅_3 as a photocatalyst is significantly weaker than that using Ag₂O or C₃N₅. In general, ESR signal intensity is positively correlated with the lone pair of electrons. Therefore, lower ESR signal intensity means a more abundant photogenerated holes (h⁺), which ascribe the more efficient separation of photogenerated carriers of Ag₂O/C₃N₅_3. From Fig. 6b, stronger ESR

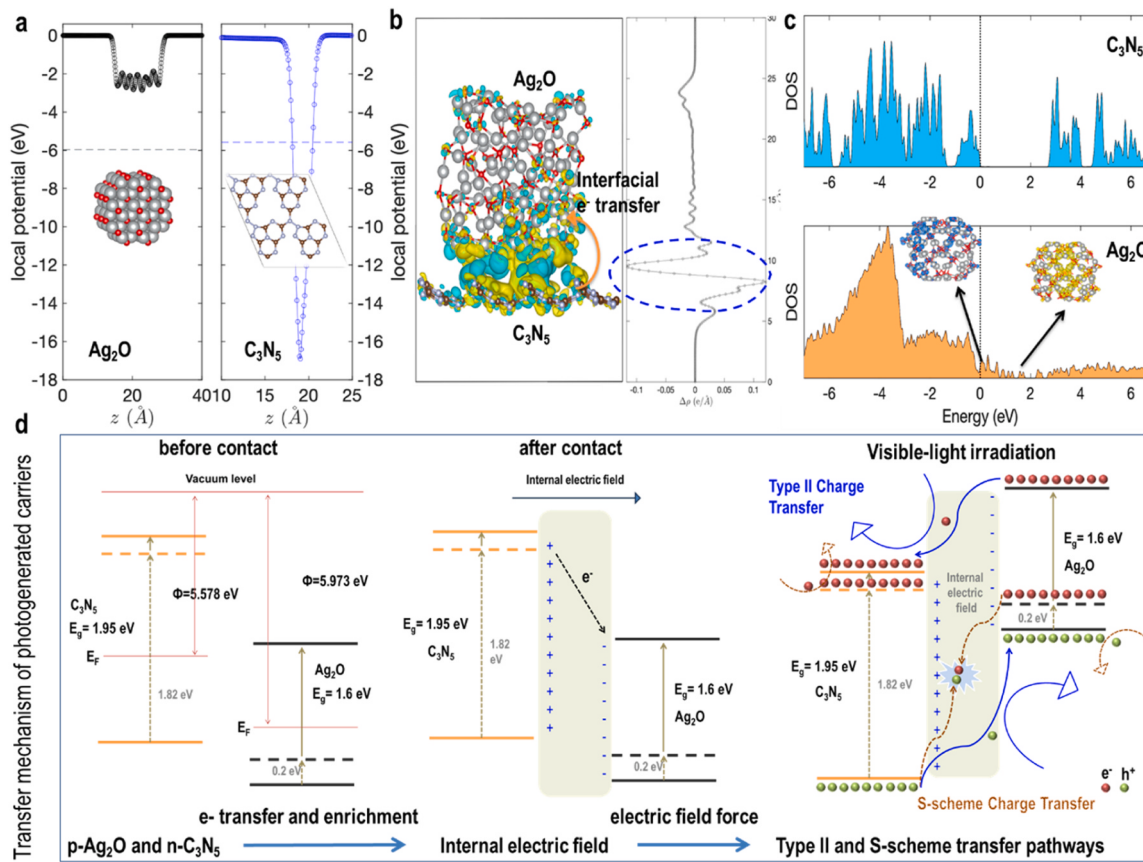


Fig. 5. (a) The local potentials of Ag₂O (left) and C₃N₅ (right). (b) Isosurfaces of charge density difference (left) and planar-average charge density plot (right) of Ag₂O/C₃N₅. Yellow and cyan clouds indicate charge gain and loss, respectively. (c) DOS plots of C₃N₅ and Ag₂O in Ag₂O/C₃N₅. The Fermi level (broken black line) is highlighted. (d) The formation procedure of dual electron transfer channels in Ag₂O/C₃N₅ heterojunction and the interfacial/bulk transfer mechanism of photo-generated carriers.

signal intensity of DMPO-•OH is observed when using Ag₂O/C₃N₅_3 than that by using Ag₂O or C₃N₅, indicating that more H₂O molecules are oxidized by increased photogenerated h⁺. Furthermore, remarkable reinforced ESR signal intensity of DMPO-•O₂ is also observed when using Ag₂O/C₃N₅_3 compared to Ag₂O or C₃N₅ (Fig. 6c), which directly demonstrates more photogenerated electrons (e⁻) produced in Ag₂O/C₃N₅_3, further reducing more O₂ molecules. Such results on one hand validate the enhanced separation efficiency of photogenerated carriers, on the other hand demonstrate the co-existence of active species including h⁺, e⁻, •O₂, and •OH in corresponding photocatalytic system.

Moreover, a series of radical burst experiments were performed to identify the dominate active species responsible for the disinfection (Fig. 6d) [13,14]. It can be observed that sequence of scavengers inhibiting the photocatalytic water disinfection performance of the Ag₂O/C₃N₅_3/Vis system is Ethylenediaminetetraacetic acid (EDTA) > tert-butylalcohol (TBA) > Furfuryl alcohol (FFA) > potassium dichromate (K₂Cr₂O₇) > 1,4-Benzoquinone (BQ). Such results clarify that h⁺ and •OH play the foremost role in photo-catalyzing water disinfection by Ag₂O/C₃N₅_3, •O₂, e⁻ and •O₂ are the secondary one. Singlet oxygen (¹O₂) shows nearly the same role with •O₂ in water disinfection. This is because that ¹O₂ is from the reaction of •O₂ oxidation by h⁺ [76].

Clearly, photoreactions of O₂ reduction by e⁻ and H₂O oxidation by h⁺ dominate the photoactivity of Ag₂O/C₃N₅ for water disinfection. It is vital to specify the reaction-site position in order to have an in-depth comprehension of anti-photocorrosion traits and enhanced efficiency. We estimated the adsorption energies of O₂ and H₂O molecules on several Ag₂O/C₃N₅ sites, including Ag₂O or C₃N₅ and the interface through detailed DFT calculations. From Fig. 6e, it can be seen that the

adsorption energies of O₂ molecule at the interface (-1.26 eV) and on C₃N₅ (-1.23 eV) are well above that (-0.05 eV) on Ag₂O, well demonstrating the fact that O₂ molecules are prefer to be reduced by photogenerated e⁻ at the interface or on C₃N₅. From Fig. 6f, the adsorption energy (-1.21 eV) of H₂O molecules at the interface is higher than that (-0.94 eV or -1.05 eV) on Ag₂O or C₃N₅, suggesting that photooxidation of H₂O molecules by h⁺ mainly occurs at the interface. Such results well support the fact that Ag₂O/C₃N₅ has an excellent anti-photocorrosion property. Furthermore, according to all above analysis, the bulk Type II charge transfer mechanism should be more important for the generation of active species •OH and •O₂. As a result, in current reaction system, the bulk Type II charge transfer mechanism is more important for the disinfection process. On the other hand, the existence of interfacial S-scheme charge transfer pathway is favorable for the reinforcement of bulk Type II charge transfer pathway. Overall, such two charge transfer pathways endow Ag₂O/C₃N₅ composite with an enhanced photocatalytic water disinfection capability.

On based of above all discussion, a possible reaction mechanism of photo-catalyzing Ag₂O/C₃N₅ heterojunction catalyst for water disinfection is proposed and illustrated in Fig. 6 g. In brief, under visible light irradiation, photogenerated e⁻ rapidly concentrate in the CB and defect sites of C₃N₅ forced by the built-in electric field through dual charge transfer channels, while the photogenerated h⁺ enrich in the VB and defect sites of Ag₂O. Subsequently, dissolved O₂ molecules are reduced by e⁻ to •O₂ at the interface or on C₃N₅, while H₂O molecules are oxidized by h⁺ to •OH at the interface or on Ag₂O. Usually, the cell membrane is widely recognized as an important protective barrier that selectively regulates the entrance of external substances while also maintaining numerous metabolic processes within the cells [17,77]. It

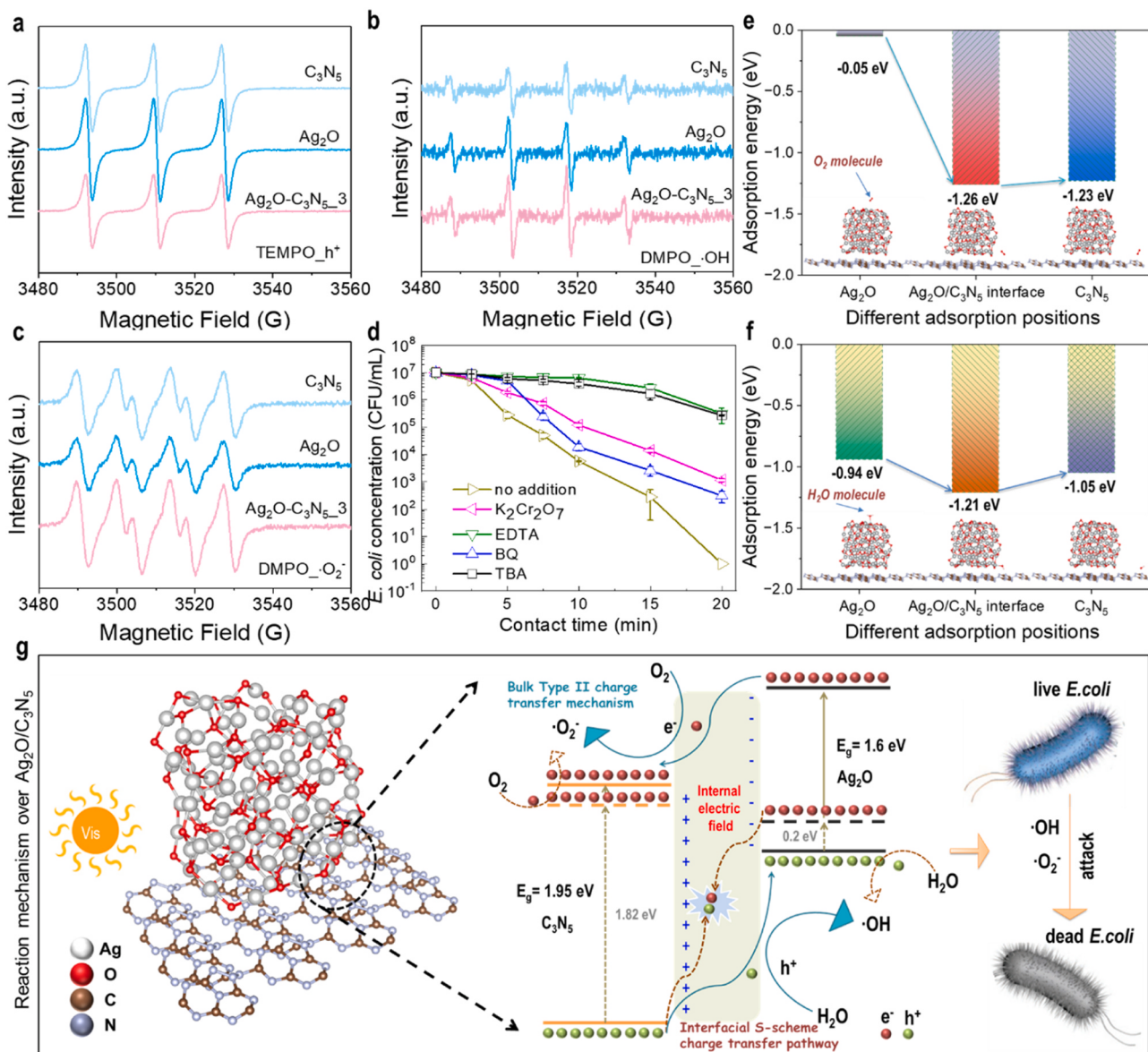


Fig. 6. (a-c) Electron-spin resonance (ESR) spectra of DMPO-O₂•-, DMPO-HO•, and TEMPO-h⁺ by using Ag₂O/C₃N₅-3, Ag₂O or C₃N₅ as a photocatalyst. (d) Influence of various active species' scavengers on the water disinfection performance of the Ag₂O/C₃N₅-3/Vis system. (e-f) Adsorption energies of O₂/H₂O molecules on Ag₂O and C₃N₅ and at the interface of Ag₂O/C₃N₅. (g) Proposed possible reaction mechanism by using Ag₂O/C₃N₅ heterojunction catalyst to photo-catalyze water disinfection under visible light.

has been demonstrated that reactive species including h⁺, •O₂, and •OH can damage cell membranes such as peptidoglycan, lipopolysaccharide, and phospholipid bilayer [17,78]. As a result, reactive species including h⁺, •O₂, and •OH generated in the reaction system will attack and damage the cell membranes of *E. coli* in water, thereby leading to the death of *E. coli*. As shown in Figure S10, it can clearly find that after 2 min of photocatalytic reaction by using Ag₂O/C₃N₅-3 as a photocatalyst, obvious red fluorescence is presented, this is because propidium iodide (PI) penetrates the damaged cell membranes of late-stage apoptotic cells and dead cells and red-stains the nuclei. Such fact well demonstrates that the photocatalytic reaction system involving Ag₂O/C₃N₅ can quickly deactivate *E. coli*, achieving good water disinfection performance.

4. Conclusion

This study for the first time reports a heterojunction catalyst with an interfacial/bulk dual charge transfer channels for water disinfection.

Driven by a built-in electric field with a direction from C₃N₅ to Ag₂O, defect energy level induced interfacial S-scheme and energy band structure determined bulk Type II charge transfer channels are formed in Ag₂O/C₃N₅ heterojunction. This unique property remarkably upgrades the separation and transfer efficiency of photogenerated carriers and achieves the spatial isolation of electrons (e⁻) and holes (h⁺), *viz.*, the former are accumulated in C₃N₅ while the latter are enriched in Ag₂O, thereby realizing the redox reaction segregation. Motivated by this, Ag₂O/C₃N₅ achieves an 7.0 folds and 1.5 folds inactivation efficiency of *E. coli* for pure C₃N₅ and Ag₂O, respectively. Furthermore, exceptional reusability are demonstrated by the renewable photoactivity and stable composition and structure caused by the anti-photocorrosion property. This study introduces a novel, efficient, and robust photocatalyst for the disinfection of water, and significantly, it puts forward and elucidates an intricate interfacial/bulk dual charge transfer mechanism.

CRediT authorship contribution statement

Junlei Zhang: Writing – review & editing, Writing – original draft, Validation, Resources, Investigation, Funding acquisition, Data curation, Conceptualization. **Chaoyang Yang:** Data curation. **Hai Liu:** Resources, Methodology, Data curation. **Guojia Yu:** Data curation. **Zhiyao Duan:** Writing – review & editing, Software, Methodology. **Shijie Li:** Writing – review & editing.

Declaration of Competing Interest

The authors declare that they have no known competing financial interests or personal relationships that could have appeared to influence the work reported in this paper

Data availability

Data will be made available on request.

Acknowledgments

This work was supported by the National Natural Science Foundation of China (No. 52300218 and 51708504) and the Natural Science Basic Research Program of Shaanxi (No. 2022JQ-334).

Appendix A. Supporting information

Supplementary data associated with this article can be found in the online version at [doi:10.1016/j.apcatb.2024.123883](https://doi.org/10.1016/j.apcatb.2024.123883).

References

- [1] R.A. Fisher, B. Gollan, S. Helaine, Persistent bacterial infections and persister cells, *Nat. Rev. Microbiol.* 15 (2017) 453–464.
- [2] M.A. Hendaus, F.A. Jomha, Covid-19 induced superimposed bacterial infection, *J. Biomol. Struct. Dyn.* 39 (2021) 4185–4191.
- [3] B. Ran, L. Ran, Z. Wang, J. Liao, D. Li, K. Chen, W. Cai, J. Hou, X. Peng, Photocatalytic antimicrobials: principles, design strategies, and applications, *Chem. Rev.* 123 (2023) 12371–12430.
- [4] W. Wang, G. Huang, J.C. Yu, P.K. Wong, Advances in photocatalytic disinfection of bacteria: development of photocatalysts and mechanisms, *J. Environ. Sci.* 34 (2015) 232–247.
- [5] L. Zhang, J. Zhang, H. Yu, J. Yu, Emerging S-scheme photocatalyst, *Adv. Mater.* 34 (2022) 2107668.
- [6] P. Zhou, J. Yu, M. Jaroniec, All-solid-state Z-scheme photocatalytic systems, *Adv. Mater.* 26 (2014) 4920–4935.
- [7] L. Ge, W. Wang, F. Tan, X. Wang, X. Qiao, P.K. Wong, Advances in photocatalytic disinfection: performances and mechanisms, *Sol. RRL* 7 (2023) 2300446.
- [8] S.I.G. Costa, V.D. Cauneto, L.D. Fiorentin-Ferrari, P.B. Almeida, R.C. Oliveira, E. Longo, A.N. Modenes, V. Slusarski-Santana, Synthesis and characterization of Nd(OH)₃-ZnO composites for application in photocatalysis and disinfection, *Chem. Eng. J.* 392 (2020) 123737.
- [9] J.M. Monteagudo, A. Duran, M.R. Martinez, I. San Martin, Effect of reduced graphene oxide load into TiO₂ P25 on the generation of reactive oxygen species in a solar photocatalytic reactor. Application to antipyrene degradation, *Chem. Eng. J.* 380 (2020) 122410.
- [10] L. Wang, F. Gao, A. Wang, X. Chen, H. Li, X. Zhang, H. Zheng, R. Ji, B. Li, X. Yu, J. Liu, Z. Gu, F. Chen, C. Chen, Defect-rich adhesive molybdenum disulfide/rGO vertical heterostructures with enhanced nanzyme activity for smart bacterial killing application, *Adv. Mater.* 32 (2020) 2005423.
- [11] R. Zhang, C. Song, M. Kou, P. Yin, X. Jin, L. Wang, Y. Deng, B. Wang, D. Xia, P. K. Wong, L. Ye, Sterilization of Escherichia coli by photothermal synergy of WO₃/C nanosheet under infrared light irradiation, *Environ. Sci. Technol.* 54 (2020) 3691–3701.
- [12] J. He, J. Cheng, I.M.C. Lo, Green photocatalytic disinfection of real sewage: efficiency evaluation and toxicity assessment of eco-friendly TiO₂-based magnetic photocatalyst under solar light, *Water Res.* 190 (2021) 116705.
- [13] L. Ni, T. Wang, K. Wang, J. Ma, Y. Wang, Novel control strategy for membrane biofouling by surface loading of aerobically and anaerobically applicable photocatalytic optical fibers based on a Z-scheme heterostructure Zr-MOFs/rGO/Ag₃PO₄ photocatalyst, *Environ. Sci. Technol.* 56 (2022) 6608–6620.
- [14] X. Chen, Z. Wang, X. Shen, Y. Zhang, Y. Lou, C. Pan, Y. Zhu, J. Xu, A plasmonic Z-scheme Ag@AgCl/PDI photocatalyst for the efficient elimination of organic pollutants, antibiotic resistant bacteria and antibiotic resistance genes, *Appl. Catal. B-Environ.* 324 (2023) 122220.
- [15] J. Li, C. Wang, S. Wu, Z. Cui, Y. Zheng, Z. Li, H. Jiang, S. Zhu, X. Liu, Superlattice nanofilm on a touchscreen for photoexcited bacteria and virus killing by tuning electronic defects in the heterointerface, *Adv. Mater.* 35 (2023) 2300380.
- [16] T. Wu, B. Liu, C. Liu, J. Wan, A. Yang, K. Liu, F. Shi, J. Zhao, Z. Lu, G. Chen, A. Pei, H.Y. Hwang, Y. Cui, Solar-driven efficient heterogeneous subminute water disinfection nanosystem assembled with fingerprint MoS₂, *Nat. Water* 1 (2023) 462–470.
- [17] X. Chen, Y. Jin, P. Huang, Z. Zheng, L.-P. Li, C.-Y. Lin, X. Chen, R. Ding, J. Liu, R. Chen, Solar driven photocatalytic disinfection by Z-scheme heterojunction of In₂O₃/g-C₃N₄: performance, mechanism and application, *Appl. Catal. B-Environ.* 340 (2024) 123235.
- [18] C. Liu, J. Zhang, W. Wang, L. Chen, M. Zhu, Progress in the synthesis and applications of N-rich carbon nitride (C₃N₅)-based catalysts in environmental and energy catalysis, *Surf. Interfaces* 42 (2023) 103491.
- [19] P. Kumar, E. Vahidzadeh, W.K. Thakur, P. Kar, K.M. Alam, A. Goswami, N. Mandi, K. Cui, G.M. Bernard, V.K. Michaelis, K. Shankar, C₃N₅: a Low bandgap semiconductor containing an Azo-linked carbon nitride framework for photocatalytic, photovoltaic and adsorbent applications, *J. Am. Chem. Soc.* 141 (2019) 5415–5436.
- [20] G.P. Mane, S.N. Talapaneni, K.S. Lakhi, H. Ilbeygi, U. Ravon, K. Al-Bahily, T. Mori, D.-H. Park, A. Vinu, Highly Ordered nitrogen-rich mesoporous carbon nitrides and their superior performance for sensing and photocatalytic hydrogen generation, *Angew. Chem. Int. Ed.* 56 (2017) 8481–8485.
- [21] J. Zhang, Z. Li, J. He, H. Tao, M. Chen, Y. Zhou, M. Zhu, Reinforced photogenerated electrons in few-layer C₃N₅ for enhanced catalytic NO oxidation and CO₂ reduction, *ACS Catal.* 13 (2023) 785–795.
- [22] K.X. Jiawei Hu, Ao Yang, Zhihao Zhang, Wen Xiao, Chao Liu, Qinfang Zhang, Interfacial engineering of ultrathin 2D/2D NiPS₃/C₃N₅ heterojunctions for boosting photocatalytic H₂ evolution, *Acta Phys. -Chim. Sin.* 40 (2024) 2305043.
- [23] C. Dong, Z.-q Wang, C. Yang, X. Hu, P. Wang, X.-q Gong, L. Lin, X.-y Li, Dual-functional single-atomic Mo/Fe clusters decorated C₃N₅ via three electron-pathway in oxygen reduction reaction for tandemly removing contaminants from water, *Proc. Natl. Acad. Sci. USA* 120 (2023) e2305883120.
- [24] S. Shi, Y. Jiang, Y. Yu, M. Liang, Q. Bai, L. Wang, D. Yang, N. Sui, Z. Zhu, Piezo-augmented and photocatalytic nanzyme integrated microneedles for antibacterial and anti-inflammatory combination therapy, *Adv. Funct. Mater.* 33 (2023) 2210850.
- [25] K.M. Alam, C.E. Jensen, P. Kumar, R.W. Hooper, G.M. Bernard, A. Patidar, A. P. Manuel, N. Amer, A. Palmgren, D.N. Puschke, N. Chaulagain, J. Garcia, P. S. Kirwin, L.C.T. Shoue, K. Cui, S. Gusalov, A.E. Kobry, V.K. Michaelis, F. A. Hegmann, K. Shankar, Photocatalytic mechanism control and study of carrier dynamics in CdS@C₃N₅ core-shell nanowires, *ACS Appl. Mater. Interfaces* 13 (2021) 47418–47439.
- [26] B. Wu, T. Sun, N. Liu, L. Lu, R. Zhang, W. Shi, P. Cheng, Modulation of Z-scheme heterojunction interface between ultrathin C₃N₅ nanosheets and metal-organic framework for boosting photocatalysis, *ACS Appl. Mater. Interfaces* 14 (2022) 26742–26751.
- [27] Z. Xiong, Y. Liang, J. Yang, G. Yang, J. Jia, K. Sa, X. Zhang, Z. Zeng, Engineering a phase transition induced g-C₃N₅/poly (triazine imide) heterojunction for boosted photocatalytic H₂ evolution, *Sep. Purif. Technol.* 306 (2023) 122522.
- [28] W. Gan, X. Fu, J. Jin, J. Guo, M. Zhang, R. Chen, C. Ding, Y. Lu, J. Li, Z. Sun, Nitrogen-rich carbon nitride (C₃N₅) coupled with oxygen vacancy TiO₂ arrays for efficient photocatalytic H₂O₂ production, *J. Colloid Interfaces Sci.* 653 (2024) 1028–1039.
- [29] F. Li, X. Yue, Y. Liao, L. Qiao, K. Lv, Q. Xiang, Understanding the unique S-scheme charge migration in triazine/heptazine crystalline carbon nitride homojunction, *Nat. Commun.* 14 (2023) 3901.
- [30] H. Dong, L. Tong, P. Zhang, D. Zhu, J. Jiang, C. Li, Built-in electric field intensified by photothermoelectric effect drives charge separation over Z-scheme 3D/2D In₂Se₃/PCN heterojunction for high-efficiency photocatalytic CO₂ reduction, *J. Mater. Sci. Technol.* 179 (2024) 251–261.
- [31] C. Li, P. Zhang, F. Gu, L. Tong, J. Jiang, Y. Zuo, H. Dong, Atomically dispersed Au confined by oxygen vacancies in Au-0-Al₂O₃/Au/PCN hybrid for boosting photocatalytic CO₂ reduction driven by multiple built-in electric fields, *Chem. Eng. J.* 476 (2023) 146514.
- [32] C. Li, Y. Zhao, Y. Song, X. Qiu, S. Wang, P. Sun, Optimization of electron transport pathway: a novel strategy to solve the photocorrosion of Ag-based photocatalysts, *Environ. Sci. Technol.* 57 (2023) 18626–18635.
- [33] T. Liu, X. Zhang, F. Zhao, Y. Wang, Targeting inside charge carriers transfer of photocatalyst: selective deposition of Ag₂O on BiVO₄ with enhanced UV-vis-NIR photocatalytic oxidation activity, *Appl. Catal. B-Environ.* 251 (2019) 220–228.
- [34] P.-L. Ji, J.-G. Wang, X.-L. Zhu, X.-Z. Kong, Preparation of silver doped TiO₂ hollow nanoparticles and characterization of their structures and photocatalytic properties, *Acta Phys. -Chim. Sin.* 28 (2012) 2155–2161.
- [35] Y. Jin, Z. Dai, F. Liu, H. Kim, M. Tong, Y. Hou, Bactericidal mechanisms of Ag₂O/TNBs under both dark and light conditions, *Water Res.* 47 (2013) 1837–1847.
- [36] N. Wei, H. Cui, Q. Song, L. Zhang, X. Song, K. Wang, Y. Zhang, J. Li, J. Wen, J. Tian, Ag₂O nanoparticle/TiO₂ nanobelt heterostructures with remarkable photo-response and photocatalytic properties under UV, visible and near-infrared irradiation, *Appl. Catal. B-Environ.* 198 (2016) 83–90.
- [37] X.-J. Wen, C.-G. Niu, L. Zhang, C. Liang, G.-M. Zeng, A novel Ag₂O/CeO₂ heterojunction photocatalysts for photocatalytic degradation of enrofloxacin: possible degradation pathways, mineralization activity and an in depth mechanism insight, *Appl. Catal. B-Environ.* 221 (2018) 701–714.

[38] H. Yu, R. Liu, X. Wang, P. Wang, J. Yu, Enhanced visible-light photocatalytic activity of Bi_2WO_6 nanoparticles by Ag_2O cocatalyst, *Appl. Catal. B-Environ.* 111 (2012) 326–333.

[39] M. Xu, L. Han, S.J. Dong, Facile fabrication of highly efficient $\text{g-C}_3\text{N}_4/\text{Ag}_2\text{O}$ heterostructured photocatalysts with enhanced visible-light photocatalytic activity, *ACS Appl. Mater. Interfaces* 5 (2013) 12533–12540.

[40] J. Zhang, B.H. Jing, Z.Y. Tang, Z.M. Ao, D.H. Xia, M.S. Zhu, S.B. Wang, Experimental and DFT insights into the visible-light driving metal-free C_3N_5 activated persulfate system for efficient water purification, *Appl. Catal. B-Environ.* 289 (2021) 120023.

[41] J. Zhang, H. Liu, Z. Ma, Flower-like $\text{Ag}_2\text{O}/\text{Bi}_2\text{MoO}_6$ p-n heterojunction with enhanced photocatalytic activity under visible light irradiation, *J. Mol. Catal. A: Chem.* 424 (2016) 37–44.

[42] P.E. Blöchl, Projector augmented-wave method, *Phys. Rev. B* 50 (1994) 17953–17979.

[43] G. Kresse, J. Hafner, Ab initio molecular dynamics for liquid metals, *Phys. Rev. B* 47 (1993) 558–561.

[44] G. Kresse, J. Hafner, Ab initio molecular-dynamics simulation of the liquid-metal-amorphous-semiconductor transition in germanium, *Phys. Rev. B* 49 (1994) 14251–14269.

[45] G. Kresse, D. Joubert, From ultrasoft pseudopotentials to the projector augmented-wave method, *Phys. Rev. B* 59 (1999) 1758–1775.

[46] J.P. Perdew, J.A. Chevary, S.H. Vosko, K.A. Jackson, M.R. Pederson, D.J. Singh, C. Fiolhais, Atoms, molecules, solids, and surfaces: applications of the generalized gradient approximation for exchange and correlation, *Phys. Rev. B* 46 (1992) 6671–6687.

[47] J. Heyd, G.E. Scuseria, M. Ernzerhof, Hybrid functionals based on a screened Coulomb potential, *J. Chem. Phys.* 118 (2003) 8207–8215.

[48] J. Heyd, J.E. Peralta, G.E. Scuseria, R.L. Martin, Energy band gaps and lattice parameters evaluated with the Heyd-Scuseria-Ernzerhof screened hybrid functional, *J. Chem. Phys.* 123 (2005).

[49] H.J. Monkhorst, J.D. Pack, Special points for Brillouin-zone integrations, *Phys. Rev. B* 13 (1976) 5188–5192.

[50] J. Zhang, H. Tao, S. Wu, J. Yang, M. Zhu, Enhanced durability of nitric oxide removal on TiO_2 (P25) under visible light: enabled by the direct Z-scheme mechanism and enhanced structure defects through coupling with C_3N_5 , *Appl. Catal. B-Environ.* 296 (2021) 120372.

[51] X. Zhou, T. Wang, L. Zhang, S. Che, H. Liu, S. Liu, C. Wang, D. Su, Z. Teng, Highly efficient $\text{Ag}_2\text{O}/\text{Na-g-C}_3\text{N}_4$ heterojunction for photocatalytic desulfurization of thiophene in fuel under ambient air conditions, *Appl. Catal. B-Environ.* 316 (2022) 121614.

[52] Z. Li, Y. Zhou, Y. Zhou, K. Wang, Y. Yun, S. Chen, W. Jiao, L. Chen, B. Zou, M. Zhu, Dipole field in nitrogen-enriched carbon nitride with external forces to boost the artificial photosynthesis of hydrogen peroxide, *Nat. Commun.* 14 (2023) 5742.

[53] J. Zhang, Z. Li, B. Liu, M. Chen, Y. Zhou, M. Zhu, Insights into the role of C-S-C bond in C_3N_5 for photocatalytic NO deep oxidation: experimental and DFT exploration, *Appl. Catal. B-Environ.* 328 (2023) 122522.

[54] I.Y. Kim, S. Kim, X. Jin, S. Premkumar, G. Chandra, N.-S. Lee, G.P. Mane, S.-J. Hwang, S. Umapathy, A. Vinu, Ordered mesoporous C_3N_5 with a combined triazole and triazine framework and its graphene hybrids for the oxygen reduction reaction (ORR), *Angew. Chem. Int. Ed.* 57 (2018) 17135–17140.

[55] H. Wang, M. Li, Q. Lu, Y. Cen, Y. Zhang, S. Yao, A mesoporous rod-like $\text{g-C}_3\text{N}_5$ synthesized by salt-guided strategy: as a superior photocatalyst for degradation of organic pollutant, *ACS Sustain. Chem. Eng.* 7 (2019) 625–631.

[56] C. Li, N. Su, H. Wu, C. Liu, G. Che, H. Dong, Synergies of adjacent sites in atomically dispersed ruthenium toward achieving stable hydrogen evolution, *Inorg. Chem.* 61 (2022) 13453–13461.

[57] C. Li, J. Zhang, X. Chen, H. Tao, Y. Zhou, M. Zhu, Upgraded charge transfer by an internal electric field in 2D/2D BiOCl/N -rich C_3N_5 heterojunctions for efficiently visible-light catalytic NO removal, *Chem. Eng. J.* 468 (2023) 143753.

[58] B. Tian, N. Wu, M. Liu, Z. Wang, R. Qu, Promoting effect of silver oxide nanoparticles on the oxidation of bisphenol B by ferrate(VI), *Environ. Sci. Technol.* 57 (2023) 15715–15724.

[59] M. Li, Q. Lu, M. Liu, P. Yin, C. Wu, H. Li, Y. Zhang, S. Yao, Photoinduced charge separation via the double-electron transfer mechanism in nitrogen vacancies $\text{g-C}_3\text{N}_5/\text{BiOBr}$ for the photoelectrochemical nitrogen reduction, *ACS Appl. Mater. Interfaces* 12 (2020) 38266–38274.

[60] J.L. Zhang, Z. Ma, $\text{AgI}/\beta\text{-Ag}_2\text{MoO}_4$ heterojunctions with enhanced visible-light-driven catalytic activity, *J. Taiwan Inst. Chem. Eng.* 81 (2017) 225–231.

[61] J. Chen, L. Lin, P. Lin, L. Xiao, L. Zhang, Y. Lu, W. Su, A direct Z-scheme $\text{Bi}_2\text{WO}_6/\text{La}_2\text{Ti}_2\text{O}_7$ photocatalyst for selective reduction of CO_2 to CO , *Chin. J. Struct. Chem.* 42 (2023) 100010.

[62] S. Li, M. Cai, Y. Liu, C. Wang, R. Yan, X. Chen, Constructing $\text{Cd}_{0.5}\text{Zn}_{0.5}\text{S}/\text{Bi}_2\text{WO}_6$ S-scheme heterojunction for boosted photocatalytic antibiotic oxidation and Cr(VI) reduction, *Adv. Powder Mater.* 2 (2023) 100073.

[63] C. Fu, T. Wu, G. Sun, G. Yin, C. Wang, G. Ran, Q. Song, Dual-defect enhanced piezocatalytic performance of C_3N_5 for multifunctional applications, *Appl. Catal. B-Environ.* 323 (2023) 122196.

[64] J. He, X. Wang, S. Jin, Z.-Q. Liu, M. Zhu, 2D metal-free heterostructure of covalent triazine framework/g- C_3N_4 for enhanced photocatalytic CO_2 reduction with high selectivity, *Chin. J. Catal.* 43 (2022) 1306–1315.

[65] H. Shang, H. Jia, W. Zhang, S. Li, Q. Wang, Q. Yang, C. Zhang, Y. Shi, Y. Wang, P. Li, Y. He, S. Xiao, D. Wang, D. Zhang, Surface hydrogen bond-induced oxygen vacancies of TiO_2 for two-electron molecular oxygen activation and efficient NO oxidation, *Environ. Sci. Technol.* 57 (2023) 20400–20409.

[66] X. Wu, B. Hu, D. Li, B. Chen, Y. Huang, Z. Xie, L. Li, N. Shen, F. Yang, W. Shi, M. Chen, Y. Zhu, Polymer photocatalysts containing segregated π -conjugation units with electron-trap activity for efficient natural-light-driven bacterial inactivation, *Angew. Chem. Int. Ed.* 62 (2023) e202313787.

[67] M. Xie, M. Gao, Y. Yun, M. Malmsten, V.M. Rotello, R. Zboril, O. Akhavan, A. Kraskouski, J. Amalraj, X. Cai, J. Lu, H. Zheng, R. Li, Antibacterial nanomaterials: mechanisms, impacts on antimicrobial resistance and design principles, *Angew. Chem. Int. Ed.* 62 (2023) e202217345.

[68] L. Wang, Z. Yang, G. Song, Z. You, X. Zhang, L. Liu, J. Zhang, L. Ding, N. Ren, A. Wang, J. Liu, H. Liu, X. Yu, Construction of S-N-C bond for boosting bacteria-killing by synergistic effect of photocatalysis and nanozyme, *Appl. Catal. B-Environ.* 325 (2023) 122345.

[69] L. Zhai, X. She, L. Zhuang, Y. Li, R. Ding, X. Guo, Y. Zhang, Y. Zhu, K. Xu, H.J. Fan, S.P. Lau, Modulating built-in electric field via variable oxygen affinity for robust hydrogen evolution reaction in neutral media, *Angew. Chem. Int. Ed.* 61 (2022) e202116057.

[70] J. Qin, Y. Dou, F. Wu, Y. Yao, H.R. Andersen, C. Hélix-Nielsen, S.Y. Lim, W. Zhang, In-situ formation of Ag_2O in metal-organic framework for light-driven upcycling of microplastics coupled with hydrogen production, *Appl. Catal. B-Environ.* 319 (2022) 121940.

[71] H. Wang, L. Zhang, Z. Chen, J. Hu, S. Li, Z. Wang, J. Liu, X. Wang, Semiconductor heterojunction photocatalysts: design, construction, and photocatalytic performances, *Chem. Soc. Rev.* 43 (2014) 5234–5244.

[72] Y. Wang, Y. Wu, X. Liu, H. Zhang, M. Zhou, L. Li, Atomic sandwiched p-n heterojunctions, *Angew. Chem. Int. Ed.* 60 (2021) 3487–3492.

[73] R. Wang, W. Yu, N. Fang, P. Wang, Y. Chu, S. Wu, J. Liang, Constructing fast charge separation of $\text{ZnIn}_2\text{S}_4@\text{CuCo}_2\text{S}_4$ p-n heterojunction for efficient photocatalytic hydrogen energy recovery from quinolone antibiotic wastewater, *Appl. Catal. B-Environ.* 341 (2024) 123284.

[74] N. Lu, X. Jing, Y. Xu, W. Lu, K. Liu, Z. Zhang, Effective cascade modulation of charge-carriers kinetics in the well-designed multi-component nanofiber system for highly-efficient photocatalytic H_2 generation, *Acta Phys. -Chim. Sin.* 39 (2023) 2207045.

[75] C. Zhai, Y. Chen, X. Huang, A.B. Isaev, M. Zhu, Recent progress on single-atom catalysts in advanced oxidation processes for water treatment, *Environ. Funct. Mater.* 1 (2022) 219–229.

[76] Z. Tang, W. Qu, Z. Lin, J. Li, P. Wu, Q. Lian, C. He, R. Yin, P.K. Wong, D. Xia, Rapid and complete inactivation of pathogenic microorganisms by solar-assisted in-situ H_2O_2 generation using a polypyrrole-supported copper sulfide system, *Appl. Catal. B-Environ.* 338 (2023) 123047.

[77] S. Rtimi, D.D. Dionysiou, S.C. Pillai, J. Kiwi, Advances in catalytic/photocatalytic bacterial inactivation by nano Ag and Cu coated surfaces and medical devices, *Appl. Catal. B-Environ.* 240 (2019) 291–318.

[78] Z. Wang, J. Li, Y. Qiao, X. Liu, Y. Zheng, Z. Li, J. Shen, Y. Zhang, S. Zhu, H. Jiang, Y. Liang, Z. Cui, P.K. Chu, S. Wu, Rapid ferroelectric-photoexcited bacteria-killing of $\text{Bi}_4\text{Ti}_3\text{O}_12/\text{Ti}_3\text{C}_2\text{T}_{\text{x}}$ nanofiber membranes, *Adv. Fiber Mater.* 5 (2023) 484–496.